

Extended main-sequence turnoffs in the double cluster  $h$  and  $\chi$  Persei: The complex role of stellar rotation

CHENGYUAN LI,<sup>1,2,3</sup> WEIJIA SUN,<sup>4,5</sup> RICHARD DE GRIJS,<sup>1,2,6</sup> LICAI DENG,<sup>3,7</sup> KUN WANG,<sup>7,8</sup> GIACOMO CORDONI,<sup>9</sup> AND ANTONINO P. MILONE<sup>9</sup>

<sup>1</sup>*Department of Physics and Astronomy, Macquarie University, Sydney, NSW 2109, Australia*

<sup>2</sup>*Centre for Astronomy, Astrophysics and Astrophotonics, Macquarie University, Sydney, NSW 2109, Australia*

<sup>3</sup>*Key Laboratory for Optical Astronomy, National Astronomical Observatories, Chinese Academy of Sciences, 20A Datun Road, Beijing 100012, China*

<sup>4</sup>*Department of Astronomy, Peking University, Yi He Yuan Lu 5, Hai Dian District, Beijing 100871, China*

<sup>5</sup>*Kavli Institute for Astronomy and Astrophysics, Peking University, Yi He Yuan Lu 5, Hai Dian District, Beijing 100871, China*

<sup>6</sup>*International Space Science Institute–Beijing, 1 Nanertiao, Zhongguancun, Hai Dian District, Beijing 100190, China*

<sup>7</sup>*Department of Astronomy, China West Normal University, Nanchong 637002, China*

<sup>8</sup>*Instituto de Astrofísica de Canarias, 38200 La Laguna, Tenerife, Spain*

<sup>9</sup>*Dipartimento di Fisica e Astronomia ‘Galileo Galilei’, Università di Padova, Vicolo dell’Osservatorio 3, IT-35122 Padova, Italy*

Submitted to ApJ

ABSTRACT

Using *Gaia* Data Release 2 photometry, we report the detection of extended main-sequence turnoff (eMSTO) regions in the color–magnitude diagrams (CMDs) of the  $\sim 14$  Myr-old double clusters  $h$  and  $\chi$  Persei (NGC 869 and NGC 884). We find that stars with masses below  $\sim 1.3 M_{\odot}$  in both  $h$  and  $\chi$  Persei populate narrow main sequences (MSs), while more massive stars define the eMSTO, closely mimicking observations of young Galactic and Magellanic Cloud clusters (with ages older than  $\sim 30$  Myr). Previous studies based on clusters older than  $\sim 30$  Myr find that rapidly rotating MS stars are redder than slow rotators of similar luminosity, suggesting that stellar rotation may be the main driver of the eMSTO. By combining photometry and projected rotational velocities from the literature of stars in  $h$  and  $\chi$  Persei, we find no obvious relation between the rotational velocities and colors of non-emission-line eMSTO stars, in contrast with what is observed in older clusters. Similarly to what is observed in Magellanic Cloud clusters, most of the extremely rapidly rotating stars, identified by their strong H $\alpha$  emission lines, are located in the red part of the eMSTOs. This indicates that stellar rotation plays a role in the color and magnitude distribution of MSTO stars. By comparing the observations with simulated CMDs, we find that a simple population composed of coeval stars that span a wide range of rotation rates is unable to reproduce the color spread of the clusters’ MSs. We suggest that variable stars, binary interactions, and stellar rotation affect the eMSTO morphology of these very young clusters.

*Keywords:* open clusters: individual: NGC 869 and NGC 884 – Hertzsprung-Russell and C-M diagrams

1. INTRODUCTION

During the last decade, a large fraction of young and intermediate-age massive clusters ( $\leq 2$  Gyr) in the Large and Small Magellanic Clouds (LMC and SMC) have been found to exhibit extended main-sequence turnoff

(eMSTO) regions (e.g., Mackey & Broby Nielsen 2007; Milone et al. 2009; Li et al. 2014, 2017; Milone et al. 2018). A similar feature was recently detected in some Galactic open clusters (OCs) by *Gaia* (Marino et al. 2018a; Cordoni et al. 2018).

A prevailing scenario to explain these eMSTOs suggests that turnoff stars in these clusters are characterized by a wide range of rotation rates (e.g., Bastian & de Mink 2009; Brandt & Huang 2015a; D’Antona et

al. 2017). First, the effect of gravity darkening caused by rapid stellar rotation would cause a rapidly rotating star to have a lower surface temperature than its non-rotating counterpart (von Zeipel 1924). In addition, individual stars will also exhibit temperature gradients on their surfaces, so that the observed colors and magnitudes depend on their inclination with respect to the line of sight. Second, rotation may increase the stellar main-sequence (MS) lifetime through expansion of the convective shell, leading to transportation of shell material to the stellar core (Maeder & Meynet 2000). As a consequence, rapid rotation will retain massive stars on the MS much longer than less massive stars, thus populating the bright extension to the MS. Finally, a range in stellar rotation rates will mimic an artificial age spread in a young cluster if we assume that all its member stars are non-rotating stars. The magnitude of this artificial age spread would be a function of the cluster’s typical age, as has been confirmed for clusters in the Magellanic Clouds (Niederhofer et al. 2015) and for Galactic open clusters (Cordoni et al. 2018).

Direct spectroscopic studies of individual stars in some young massive clusters have shown that rapidly rotating stars are generally redder than slowly or non-rotating stars (Dupree et al. 2017; Marino et al. 2018a,b). In addition, a survey of Be stars in young LMC clusters has confirmed that Be stars, which are supposed to be rotating at near-critical rotation rates, are systematically redder than normal MS stars (Milone et al. 2018). Stars in Galactic OCs have been reported to exhibit a large range of rotation rates (Huang & Gies 2006; Huang et al. 2010). A number of studies have explored how stars with different rotation rates will populate their clusters’ turnoff regions (e.g., Brandt & Huang 2015b). However, only a limited number of studies have revealed direct correlations between the rotation rates exhibited by turnoff stars and their distributions in cluster color–magnitude diagrams (CMDs) (Bastian et al. 2018; Marino et al. 2018a).

In this paper, we study the turnoff and upper-MS stars of the double clusters  $h$  and  $\chi$  Persei (NGC 869 and NGC 884). We aim to explore the correlation, if any, between their rotational velocities and the stellar color–magnitude distributions. We combine photometry from *Gaia* Data Release 2 (DR2; Gaia Collaboration et al. 2016, 2018) and the stellar catalog of Huang & Gies (2006); Huang et al. (2010), which includes information about the rotation rates of individual stars in our sample clusters.

We obtained the photometric stellar catalog from the *Gaia* archive<sup>1</sup>. Based on the parameters provided by Kharchenko et al. (2013), we adopted radii of, respectively, 3,050 arcsec and 3,500 arcsec as the areas to search for stars associated with  $h$  and  $\chi$  Persei. These areas are slightly larger than their tidal radii. The resulting stellar catalog contains 143,900 and 187,596 stars associated with the regions occupied by  $h$  and  $\chi$  Persei, respectively, for which we have information about (1) the spatial coordinates (right ascension and declination), (2) parallaxes, (3) proper motions, and (4) photometry (in the  $G_{\text{bp}}$ ,  $G_{\text{rp}}$ , and  $G$  passbands). We first removed all stars associated with unrealistic negative parallaxes. These stars may have been affected by confusion in the observation-to-source matching, and they will have unreliable proper motions (Gaia Collaboration et al. 2018). This step led to the removal of  $\sim 32\%$  of the stars from the raw stellar catalog. Because  $h$  and  $\chi$  Persei are located in close vicinity to each other, their cluster regions as defined by their tidal radii overlap. We further removed 77,227 stars that appeared as duplicates in both clusters’ stellar catalogs and combined them into a common catalog. Finally, 147,748 stars were located in the area containing both clusters.

To decontaminate the field stars, we explored the proper motion map of all stars. We calculated their density contours across the entire proper-motion diagram. We found that there is a clearly overdense region centered at about  $\mu_{\alpha_{J2000}} \cos \delta = -0.65 \text{ mas yr}^{-1}$  and  $\mu_{\delta_{J2000}} = -1.05 \text{ mas yr}^{-1}$ , which corresponds to the bulk motions of both  $h$  and  $\chi$  Persei, where  $\mu_{\alpha_{J2000}}$  and  $\mu_{\delta_{J2000}}$  are the angular velocities of the stellar proper motions in the right ascension and declination directions, and  $\delta$  is the declination. We did not find any significant differences between the proper motions of  $h$  and  $\chi$  Persei. Our results are well-matched with literature results for  $h$  and  $\chi$  Persei (Cantat-Gaudin et al. 2018). The proper-motion map for all stars, as well as the calculated number density contours, are shown in Figure 1. We selected all stars located within the area enclosed by the isodensity contour representing  $25,000 \text{ yr}^{-2} \text{ mas}^{-2}$  (see the red line in Figure 1) as candidate cluster stars. This selection removed 95% of all detected stars, leaving only 7,452 stars.

In Figure 2 we present the spatial distribution of all 7,452 stars in our final selection. They exhibit two clear clumps centered at  $\alpha_{J2000} \sim 34.75 \text{ deg}$  ( $2^{\text{hh}}19^{\text{mm}}0.12^{\text{ss}}$ ),  $\delta_{J2000} \sim 57.15 \text{ deg}$  ( $57^{\circ}9'0.00''$ ) and  $\alpha_{J2000} \sim 35.52 \text{ deg}$  ( $2^{\text{hh}}22^{\text{mm}}4.80^{\text{ss}}$ ),  $\delta_{J2000} \sim 57.14 \text{ deg}$  ( $57^{\circ}8'24.00''$ ).

## 2. DATA REDUCTION

<sup>1</sup> <http://gea.esac.esa.int/archive/>

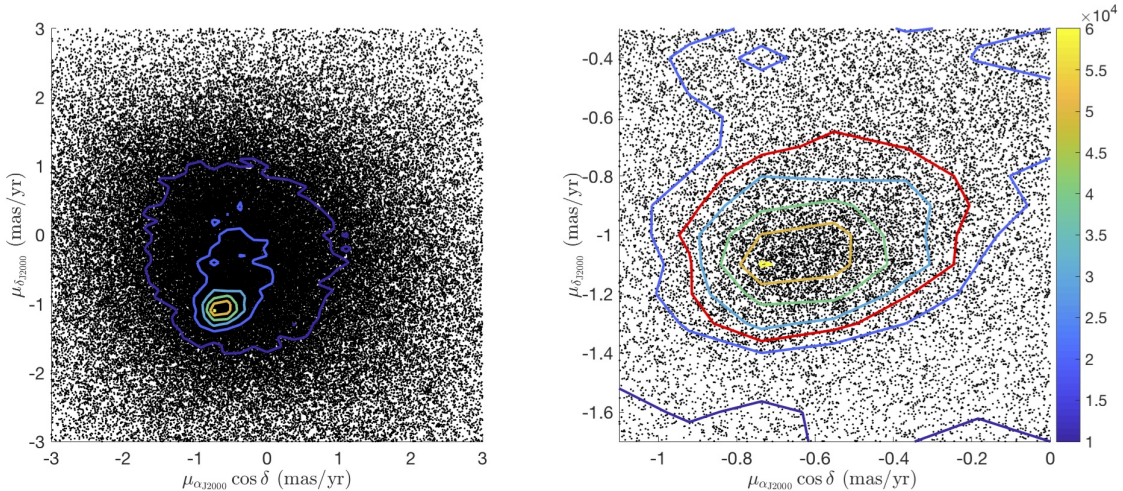


**Figure 1.** Proper-motion diagrams of stars in the search area for the clusters  $h$  and  $\chi$  Persei. Overplotted are contours representing stellar number densities (in units of  $N \text{ deg}^{-2}$ ). The right-hand panel exhibits a zoomed-in region. Stars located in the red loop (i.e., the isodensity loop for  $25,000 \text{ yr}^2 \text{ mas}^{-2}$ ) were selected as candidate cluster stars.

These results are generally consistent with those of Wu et al. (2009). We plot their number density contours by assigning all stars to 1,196 spatial grid cells ( $46 \times 26$  cells in  $[\alpha_{J2000}, \delta_{J2000}]$  space) and calculated the average stellar number density in each cell. At the edge of the region, the average stellar number density is  $\sim 56,000 \text{ deg}^{-2}$ , while in the central region, the isodensity contour associated with a stellar number density of  $\sim 3 \times 10^5 \text{ deg}^{-2}$  shows two distinct closed loops, indicating that both clusters are clearly separated at this number density level. We thus selected stars located within these two loops (see the red and blue lines in Figure 2) to represent the  $h$  and  $\chi$  Persei subsamples. Thus, we identified 828 and 720 stars in  $h$  and  $\chi$  Persei, respectively, as shown in Figure 2 (red and blue dots, respectively).

OCs located in the dusty Galactic disk may be severely affected by reddening. Spatially variable extinction (differential reddening) will introduce uncertainties in the actual colors and magnitudes of member stars located in different parts of an OC, thus potentially mimicking an artificial eMSTO. However, only a small number of stars brighter than  $G = 17$  mag have associated reddening values in the *Gaia* DR2 photometric catalog. Therefore, we used the Galactic Dust Reddening and Extinction service provided by the NASA/IPAC Infrared Science Archive<sup>2</sup> (Schlafly & Finkbeiner 2011) to correct our cluster photometry for differential reddening effects. We aim to correct all 7,452 stars for differential reddening. Because the typical spatial resolution of the Galactic Dust Reddening and Extinction service is  $5'$ , we examined the average extinction,  $E(B - V)$ , for  $16 \times 17$  adja-

cent circular regions with radii of  $5'$  in  $[\alpha_{J2000}, \delta_{J2000}]$  space.

The reddening is higher in the north and east and lower in the south and west, as shown in Figure 3 (indicated by the color-coded background). We confirmed this apparent reddening gradient by visually inspecting an Infrared Astronomical Satellite (IRAS)  $100 \mu\text{m}$  image<sup>3</sup> as well. We then calculated the individual stellar extinction values by matching their spatial coordinates with the derived reddening map. All cluster stars are subject to reddening ranging from  $A_V = 0.98$  mag to  $A_V = 2.41$  mag; 95% (7,164 stars) have reddening values between  $A_V = 1.10$  mag and  $A_V = 2.27$  mag, with an average reddening value of  $A_V = 1.59$  mag. As regards the  $h$  and  $\chi$  Persei subsamples, their average reddening and dispersion (covering 95% of all stars) are  $A_V = 1.49^{+0.15}_{-0.14}$  mag and  $A_V = 1.60^{+0.18}_{-0.11}$  mag, respectively.  $\chi$  Persei is subject to higher average reddening than  $h$  Persei, which is expected given its location on the eastern side of  $h$  Persei since the IRAS  $100 \mu\text{m}$  image has revealed that this region is very dusty.

Finally, we corrected our stellar photometry to represent the average reddening using the Cardelli et al. (1989) and O'Donnell (1994) extinction curve with  $R_V = 3.1$ . In Figure 4 we show the CMDs of all stars before (left) and after (right) correcting for differential reddening. A clear color gradient is seen across the entire CMD if differential reddening is not corrected for, with stars affected by higher reddening being systemati-

<sup>3</sup> <https://irsa.ipac.caltech.edu/Missions/iras.html>

<sup>2</sup> <https://irsa.ipac.caltech.edu/applications/DUST/>

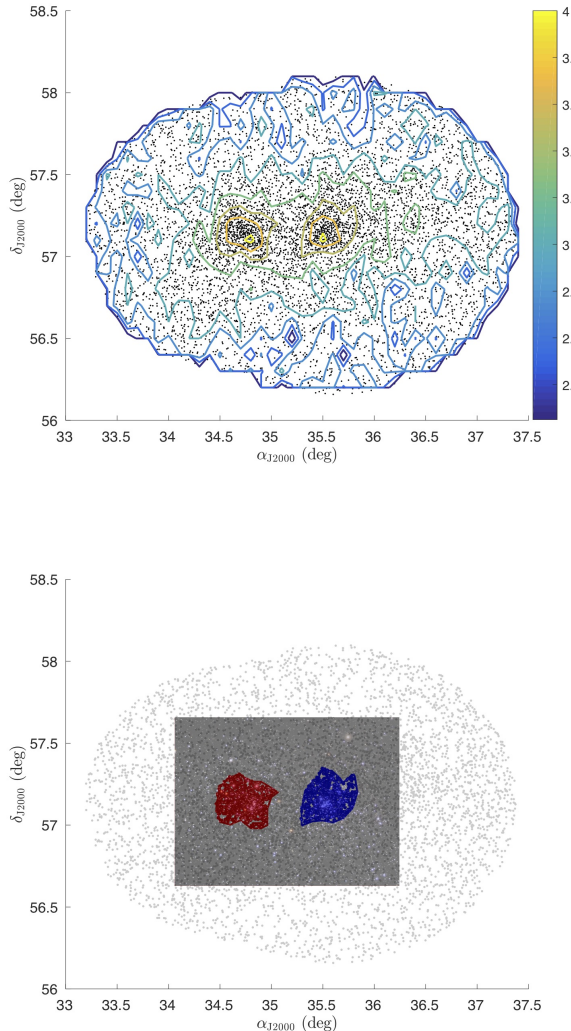


**Figure 2.** (top) Spatial distributions of the proper-motion-selected stars in our search area, as well as their number density contours ( $\log(N\text{deg}^{-2})$ ). (bottom) Spatial distribution of all selected stars, superimposed on the real color image background (N. A. Sharp/NOAO/AURA/NSF). Stars associated with  $h$  and  $\chi$  Persei are highlighted by red and blue dots, respectively.

cally redder than stars affected by less reddening. After correction, this color gradient all but disappears.

### 3. RESULTS

The differential-reddening-corrected CMDs of  $h$  and  $\chi$  Persei are presented in Figure 5. Our results exhibit clear similarities to the CMDs of young clusters in the Magellanic Clouds (e.g., Milone et al. 2015, 2016, 2018). Stars fainter than  $G \sim 15.5$  mag populate a narrow MS and a clear binary envelope, while the upper MS and MSTO exhibit clear color spreads which make the binary envelope less distinct. There is an internal color-

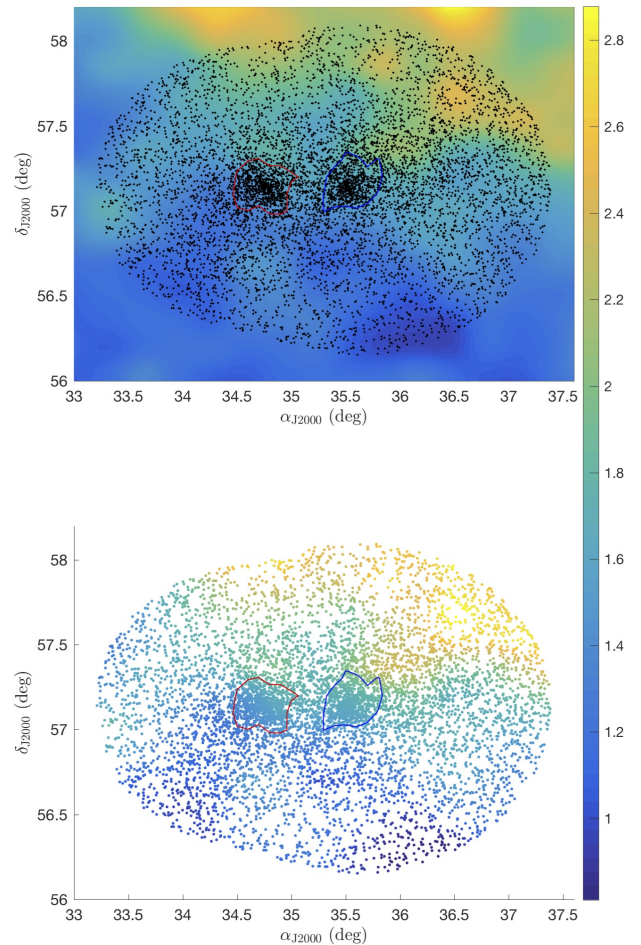


**Figure 3.** (top) Spatial distributions of stars overplotted on the reddening atlas, as indicated by the color bar (in mag). (bottom) Spatial distributions of stars with their interpolated reddening values color-coded. Red and blue loops are the boundaries defined for the subsamples coinciding with  $h$  and  $\chi$  Persei, respectively.

magnitude spread for stars with  $G \leq 15.5$  mag. These stars map onto a complex morphology of the upper MS and the MSTO regions in the CMDs of  $h$  and  $\chi$  Persei.

Because differential stellar distances may also broaden the MS, we calculated the individual stellar distance moduli based on parallax measurements. The average distance to  $h$  and  $\chi$  Persei was previously reported as about 2.3 kpc (Kharchenko et al. 2013). In the bottom panel of Figure 5, we plot the corresponding CMDs for all stars with distances between 2.0 and 2.6 kpc. This distance range corresponds to a parallax spread of  $\pm 0.05$  mas. However, we emphasize that this selection might

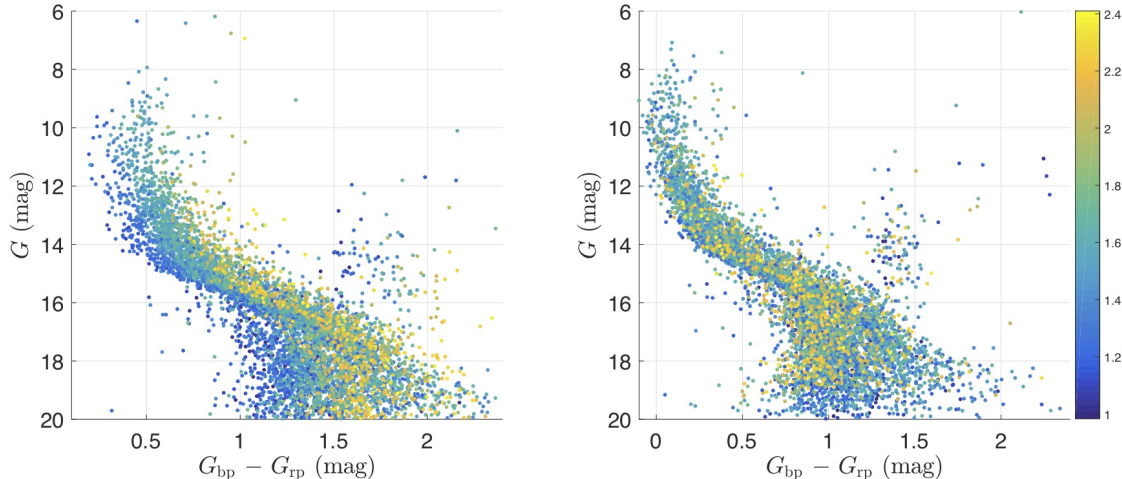


**Figure 4.** (left) Raw CMD of all proper-motion-selected stars in the search area. (right) Differential reddening corrected CMD for all stars. The color bar indicates the interpolated reddening for individual stars.

be too strict for the stars of interest, since the typical parallax uncertainty for stars of  $G \sim 15.5$  mag is 0.04–0.1 mas (Gaia Collaboration et al. 2018). As shown in Figure 5, even though we have set strict constraints on the distance range of our stellar sample, the extended MSs and MSTOs are still obvious. No obvious gradient in mean magnitude for stars at different distances was detected in either of these CMDs.

We next used the MESA Isochrone and Stellar Tracks (MIST Paxton et al. 2011, 2013, 2015; Choi et al. 2016; Dotter 2016) models to generate different isochrones to fit the observations. (Slesnick et al. 2002) derived an age of  $\sim 13$  Myr and solar metallicity for both  $h$  and  $\chi$  Persei. Our fits agree with their results. To describe the blue boundary and the knee of the MS ( $G \sim 15$ – $16$  mag), the best-fitting isochronal age and metallicity for both  $h$  and  $\chi$  Persei are 13.8 Myr and solar metallicity ( $Z = 0.0142$  in the MIST models), respectively. Using the parallaxes from Gaia DR2, we recalculated the average distance moduli for both  $h$  and  $\chi$ , resulting in  $(m - M)_0 = 11.69$  mag and 11.81 mag, respectively. The adopted average reddening values for the clusters are  $A_V = 1.49$  mag and  $A_V = 1.60$  mag, respectively. We assumed that the average stellar rotation rate was close to zero.

This age of the best-fitting isochrone can be constrained by an A-type star located in the red portion of the Hertzsprung gap of  $h$  Persei and an M supergiant star in  $\chi$  Persei (see the red pentagrams in Figure 6). However, these isochrones only describe the blue edge of the upper MSs and the MSTOs of  $h$  and  $\chi$  Persei. They do not describe the red part of the MSs, as expected. The color spreads of stars in the upper MS and MSTO regions of  $h$  and  $\chi$  Persei (for  $G \leq 15.5$  mag) are about  $\Delta(B_{\text{bp}} - B_{\text{rp}}) \sim 0.25$  mag. The average pho-

tometric uncertainties for stars in this magnitude range are  $\delta B_{\text{bp}} \leq 0.006$  mag and  $\delta B_{\text{rp}} \leq 0.004$  mag (Evans et al. 2018, their Figures 10 and 11), which translates into a color uncertainty of  $\delta(B_{\text{bp}} - B_{\text{rp}}) \leq 0.007$  mag. The observed color spread is about 35 times the theoretical color uncertainty. The possibility that the extended upper MS and MSTO regions are caused by photometric uncertainties is therefore negligible. The extended upper MS is unlikely to have been caused by unresolved binaries either, since the upper range of the MS is almost vertical in the CMD. In Figure 6, we present the observed CMDs of  $h$  and  $\chi$  Persei and the best-fitting isochrones, as well as the loci of the equal-mass unresolved binaries.

To quantify the width of the clusters’ eMSTO regions, we next obtained fits using older isochrones characterized by the same metallicity and extinction to describe the red part of the MSs. We found that even an older isochrone with an age of  $\sim 100$  Myr (see the red lines in Figure 6) cannot satisfactorily describe the morphology of the upper MS. These isochrones (with ages of  $\sim 14$  Myr and 100 Myr) can only reproduce the MS for  $G \leq 12$  mag, while the observed MSs show clear color spreads at  $G \leq 15$  mag. If these color spreads are caused by genuine age spreads, we should expect well-populated red giant branches in both young clusters, but this is not observed. In summary, although fits of single stellar populations to the observations are inadequate, the clusters’ eMSTO regions and broadened MSs are unlikely caused by significant age spreads among their member stars.

An alternative explanation, prevailing for most young clusters exhibiting eMSTO regions (e.g., Niederhofer et al. 2015; D’Antona et al. 2017; Dupree et al. 2017;

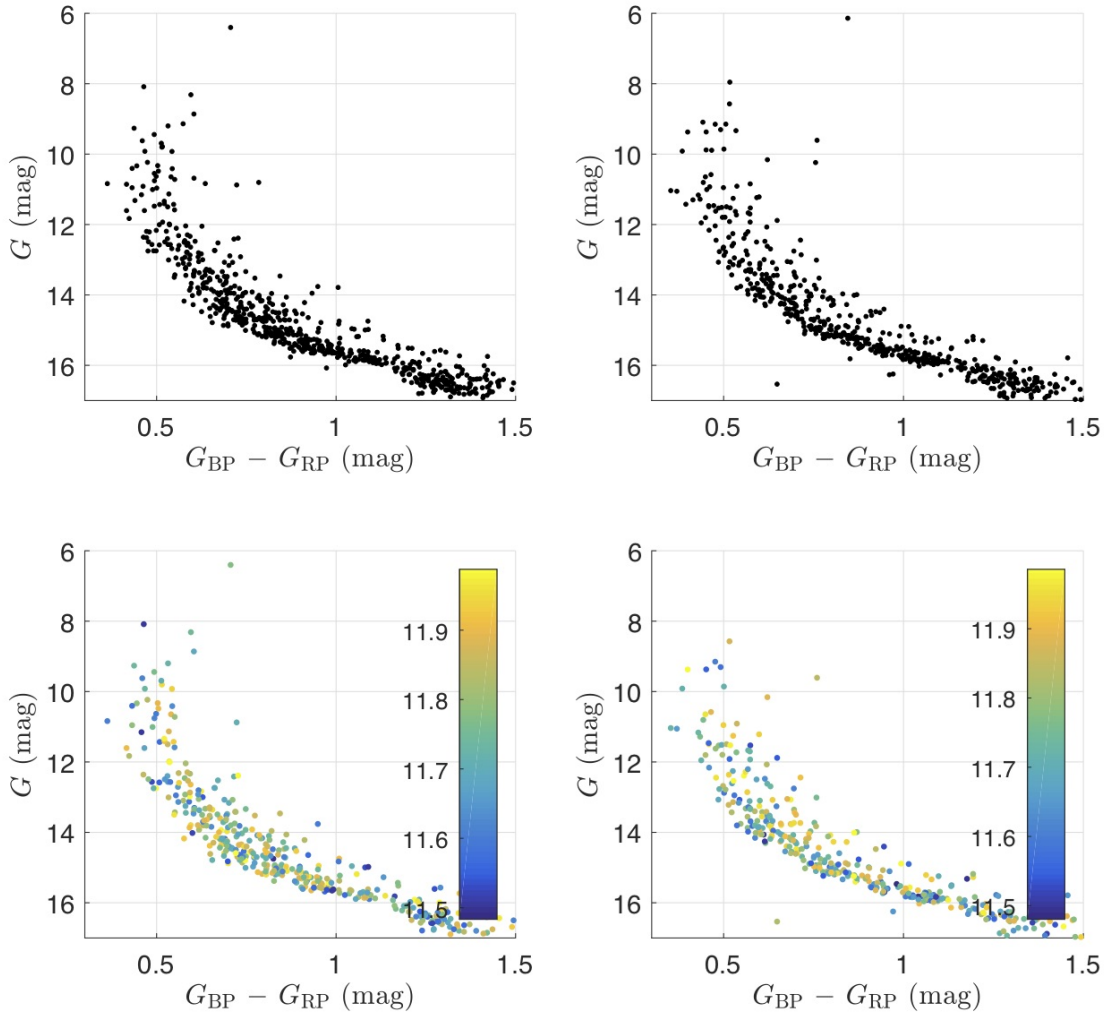


**Figure 5.** Differential-reddening-corrected CMDs composed of stars in  $h$  and  $\chi$  Persei (left and right, respectively). The corresponding bottom panels show the distance-constrained CMDs, as indicated by the color bars.

Marino et al. 2018a, however, see Goudfrooij et al. (2017, 2018); Piatti & Cole (2017)), invokes stellar rotation. This scenario suggests that the color–magnitude spread of MS and MSTO stars may be caused by differences in the cluster stars’ rotation rates. Specifically, the gravity darkening caused by different stellar rotation rates and inclinations will render different stellar colors and luminosities. Rotational mixing would prolonge the MS lifetimes of rapidly rotating stars, resulting in MSTO stars of different masses (Yang et al. 2011). All of these effects cause stellar rotation to play a complex role in shaping the morphology of a cluster’s MSTO region.

To address whether stellar rotation is the underlying cause of the eMSTOs of  $h$  and  $\chi$  Persei, a direct comparison with models is required. To do so, we requested syn-

thetic photometry representative of a simple stellar population from the SYCLIST model suite<sup>4</sup> (Georgy et al. 2014) for different rotation rates. The requested model contains 5000 single stars and 5000 unresolved binary systems at a fixed age of 14 Myr ( $\log t/\text{yr} = 7.15$ ) and for solar metallicity ( $Z = 0.014$ ), characterized by the empirical stellar rotational velocity distribution of Huang et al. (2010). For rapidly rotating stars, both gravity darkening and limb darkening are considered (Espinosa Lara & Rieutord 2011). Photometric data points for our simulated cluster are given in the standard Johnson–Cousins  $UBVRI$  photometric system. Using color–color mapping between the Johnson–Cousins passbands and

<sup>4</sup> <https://www.astro.unige.ch/syclist/index/Formats/#cluster>

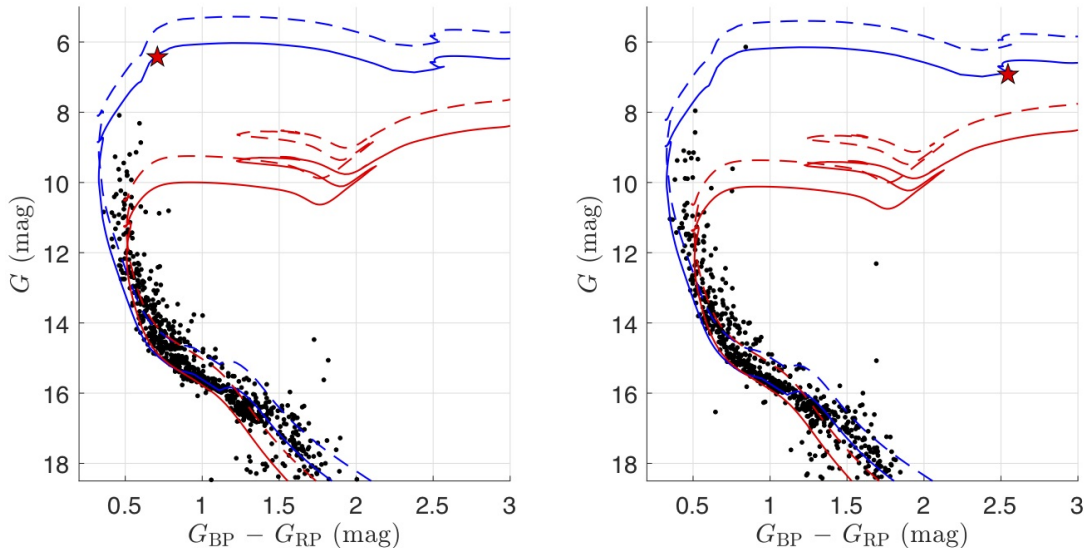


**Figure 6.** Distance-constrained, differential-reddening-corrected CMDs of stars in  $h$  and  $\chi$  Persei (left and right, respectively), fitted by isochrones with ages of 14 Myr (blue solid lines) and 100 Myr (red solid lines). The dashed lines are the corresponding loci for unresolved, equal-mass binaries. Red stars are the A-type turnoff star ( $h$  Persei) and the M supergiant star ( $\chi$  Persei) used to determine the best fits of the younger isochrones.

the *Gaia* photometric system provided by the *Gaia* DR2 documentation<sup>5</sup>, we calculated the corresponding *Gaia* photometry in the  $G$ ,  $G_{\text{BP}}$ , and  $G_{\text{RP}}$  passbands.

Similarly as in [Cordoni et al. \(2018\)](#), in Figure 7 we show the CMDs of the observed cluster stars as well as a set of simulated CMDs for non-rotating and rapidly rotating populations. For clarity, the simulated stars do not contain any unresolved binaries and their photometry is noise-free. Although the rapidly rotating stars exhibit some spread in their color–magnitude distributions, the observed widths of the MSTO regions are still much wider than those resulting from the simulations.

For a more realistic assessment, we modeled a synthetic stellar population characterized by various stellar rotation rates and added realistic observational noise to each star’s photometry to mimic the effects of both photometric uncertainties and possible differential reddening residuals. We added similar photometric uncertainties to our stellar photometry as in the observations. Although we corrected the individual stellar photometry for differential reddening, we are aware of the fact that a residual reddening spread may introduce a color–magnitude spread in the CMD. Indeed, even though we added realistic photometric uncertainties to our simulation, the simulated MS is still narrower than the observed MSs for  $G \geq 15.5$  mag. These additional MS spreads may be caused by reddening residuals. Fi-

nally, we included additional photometric uncertainties of  $\delta G \sim 0.006$  mag and  $\delta(G_{\text{BP}} - G_{\text{RP}}) \sim 0.009$  mag to our simulation to reproduce the spread caused by this residual differential reddening.

Figure 8 shows the CMDs of both the synthetic clusters and the observations. For the synthetic clusters, we use a range in color to represent their projected rotational velocities ( $V \sin i$ ). For a stellar population of only 14 Myr old, the color distribution of the MSTO stars does not depend on their rotational velocities. This is different from the situation for the clusters M11 and NGC 2818, as reported by [Marino et al. \(2018a\)](#) and [Bastian et al. \(2018\)](#), whose upper MS and MSTO stars show a clear correlation between their colors and the projected rotational velocities: the rapid rotators preferentially occupy the red parts of the MSTO regions. This is so, because rotational mixing has prolonged the MS lifetimes of the rapidly rotating stars, which masks the effects of gravity darkening. In turn, this causes their color–magnitude distribution to define an MSTO locus that is almost indistinguishable from that of the non-rotating stars. In addition, the model implies that the color spread of stars with different rotational velocities is still too small to reproduce the observations. This is because for a stellar population of only 14 Myr old, the upper MS and MSTO stars are too hot to show clear color differences owing to gravity darkening when comparing extremely rapidly rotating stars with their non-rotating counterparts.

<sup>5</sup> <http://gea.esac.esa.int/archive/documentation/GDR2/>

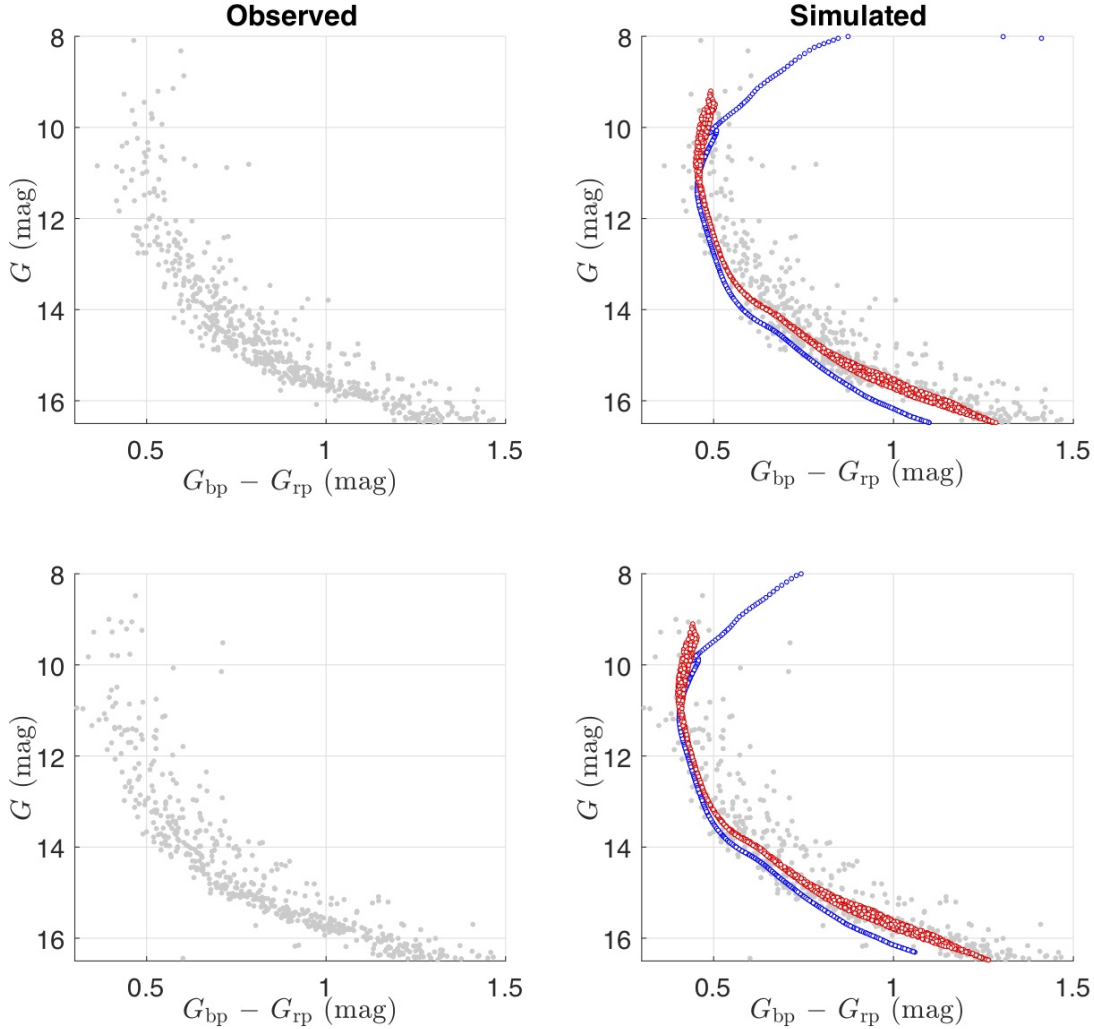


**Figure 7.** Observed CMDs of (top left) NGC 869 and (bottom left) NGC 884, as well as (right) the corresponding simulated CMDs pertaining to non-rotating (blue) and rapidly rotating (for  $\omega = 0.9\omega_{\text{cr}}$ , red) populations.

We used the stellar catalogs provided by Huang & Gies (2006) and Huang et al. (2010). These catalogs contain 89 and 95 stars located in the areas of, respectively,  $h$  and  $\chi$  Persei, with their projected rotational velocities calculated by comparison of moderate-resolution observational spectra with synthetic spectra calculated by TLUSTY and SYNSPEC (Hubeny & Lanz 1995). Specifically, they fitted the observed absorption line profiles to the synthetic rotational profiles across a grid of projected rotational velocities (see Figure 1 of Huang & Gies 2006, as an example). We cross-matched these stars with our proper-motion-selected samples. However, we remind reader that some of their sample objects are located beyond the cluster regions we have adopted. Nevertheless, we still use these stars in order to attain

a larger sample. We selected, respectively, 56 and 64 stars in common for  $h$  and  $\chi$  Persei from both our catalog and those of Huang & Gies (2006) and Huang et al. (2010). The latter stellar catalogs also include information about double-lined spectroscopic binaries, radial velocity variables (possible binaries), and H $\alpha$  emission-line (Be) stars. Stars with unusual line profiles were removed because the measurements of their projected rotational velocities may be unreliable. Finally, 40, 11, and three stars were identified as normal stars, binaries (including both confirmed double-lined spectroscopic binaries and radial velocity variables), and emission-line stars in  $h$  Persei, while for  $\chi$  Persei the corresponding numbers are 39, 16, and five.



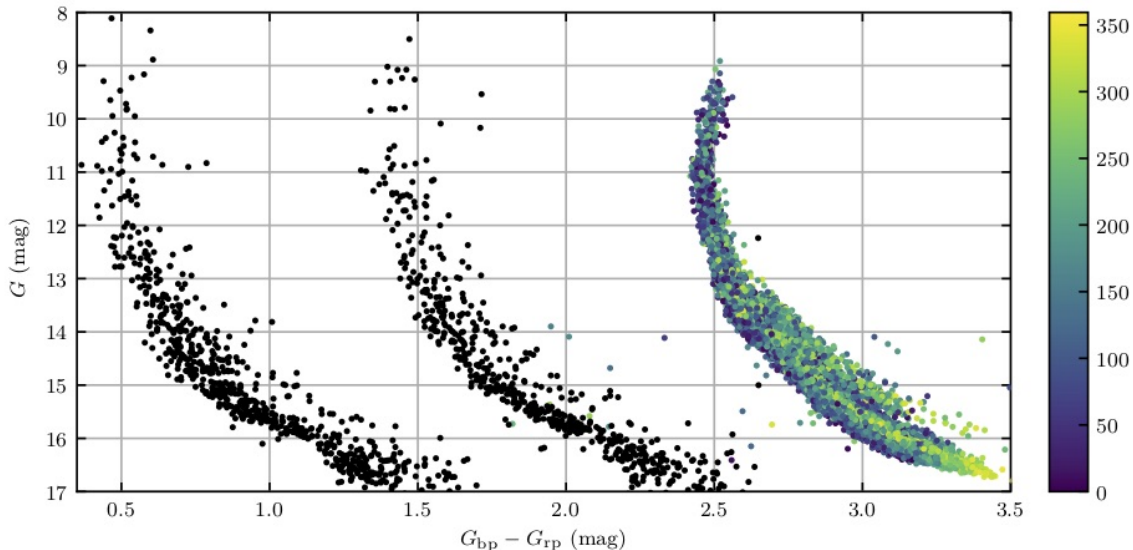


**Figure 8.** CMDs of our observations (black circles) and the synthetic cluster (colored dots), with their  $V \sin i$  indicated by the color bar (in  $\text{km s}^{-1}$ ). To visually highlight the similarities and differences between the observations and the synthetic cluster, NGC 884 (middle) and the model cluster (right) have been shifted in color.

In Figure 9 we show the CMDs of  $h$  and  $\chi$  Persei, along with the measured  $V \sin i$  values for the subsamples’ normal stars and binaries (enclosed in squares), as indicated by the color bar. Indeed, no obvious correlation between the projected rotational velocities and the color–magnitude distributions was detected in either cluster. However, most of the Be stars are located in the red part of the MS (see the red triangles in Figure 9). This is similar to the case for young clusters in the LMC (Milone et al. 2018). Since Be stars are thought to be extremely rapidly rotating stars with near-critical rotation rates, the fact that Be stars are systematically redder than normal stars may indicate that stellar rotation still plays a role in the eMSTO regions of  $h$  and  $\chi$  Persei.

Figures 10 and 11 show the  $\Delta(G_{\text{bp}} - G_{\text{rp}}) - V \sin i$  distributions for all of our stars. Here,  $\Delta(G_{\text{bp}} - G_{\text{rp}})$  is the stellar color deviation with respect to the zero-age MS (ZAMS) described by the best-fitting, 14 Myr-old isochrones. Stars located in the middle of the upper MS exhibit the largest velocity dispersion. A major fraction of stars located in the red portion of the ZAMS, with  $\Delta(G_{\text{bp}} - G_{\text{rp}}) \sim 0.07\text{--}0.15$  mag, cover the full spectrum of projected rotational velocities, ranging from zero to  $\sim 360$   $\text{km s}^{-1}$ . Most stars located close to the ZAMS, with  $\Delta(G_{\text{bp}} - G_{\text{rp}}) \leq 0.07$  mag, have projected rotational velocities of less than  $200$   $\text{km s}^{-1}$ . Only two exceptions exhibit projected rotational velocities of  $\sim 400$   $\text{km s}^{-1}$ . Stars located in the red part of the MS, with  $\Delta(G_{\text{bp}} - G_{\text{rp}}) \sim 0.15\text{--}0.25$  mag, exhibit a distribution

of projected rotational velocities from almost zero to  $\sim 300$   $\text{km s}^{-1}$ . Seven stars have  $\Delta(G_{\text{bp}} - G_{\text{rp}}) \geq 0.25$  mag, four of which are identified as emission-line stars. There are no significant differences between the distributions of possible binaries (blue circles and squares) and normal stars (red circles and squares). Similarly to Marino et al. (2018a), we calculated the Spearman’s correlation coefficient between  $\Delta(G_{\text{bp}} - G_{\text{rp}})$  and  $V \sin i$ . Marino et al. (2018a) found a clear correlation between the colors and the projected rotational velocities of eMSTO stars in M11, characterized by a Spearman’s correlation coefficient of  $c = 0.55$ . For NGC 869 and NGC 884 we only find  $c = 0.22$  and  $0.04$ , respectively.

Using the same method as applied to the observations, for each simulated star we calculated  $\Delta(G_{\text{BP}} - G_{\text{rp}})$  with respect to the 14 Myr-old isochrone. For the observations, the best-fitting isochrone describes the blue edge of the eMSTO (Figure 6), while for the simulation, the isochrone is of course the ridge-line. This means that the zeropoint for the observed  $\Delta(G_{\text{bp}} - G_{\text{rp}})$  distribution is different from that for the simulation. After having corrected the zeropoint difference to coincide with the observations, we compared the  $\Delta(G_{\text{BP}} - G_{\text{rp}}) - V \sin i$  distributions. We only examined the 1,785 simulated stars with  $G \leq 13.5$  mag. None have  $\Delta(G_{\text{BP}} - G_{\text{rp}}) \geq 0.25$  mag, while more than 91% have  $\Delta(G_{\text{BP}} - G_{\text{rp}}) \leq 0.15$  mag. For comparison, 4–10% of stars have  $\Delta(G_{\text{BP}} - G_{\text{rp}}) \geq 0.25$  mag (2 of 56 and 7 of 64 in NGC 869 and NGC 884, respectively). In addition, 34–36% (19 of 56 and 23 of 64) have

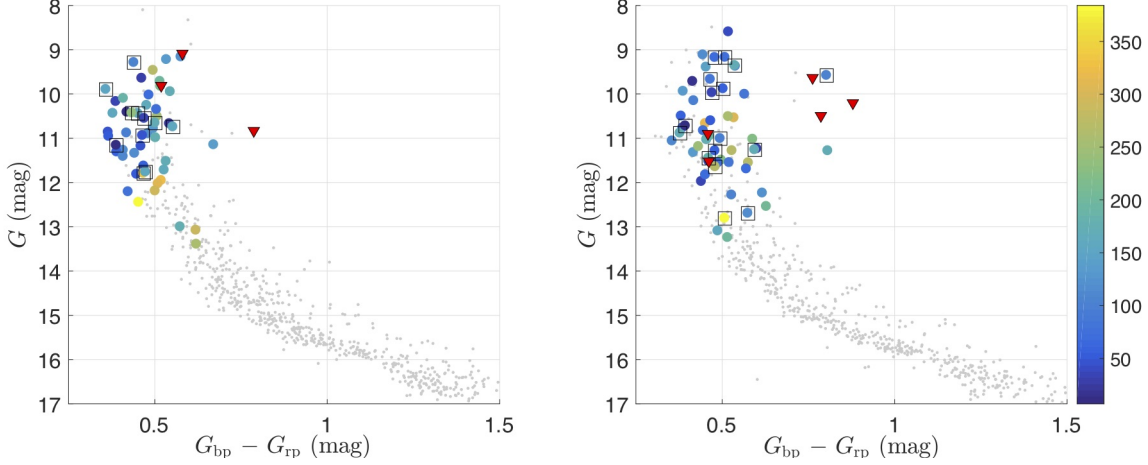


**Figure 9.** Color–magnitude distributions of stars with measured projected rotational velocities,  $V \sin i$ , as indicated by the color bar (in  $\text{km s}^{-1}$ ). Double-lined spectroscopic binaries and radial velocity variables (possible binaries) are highlighted in squares. Red triangles are stars showing emission lines.

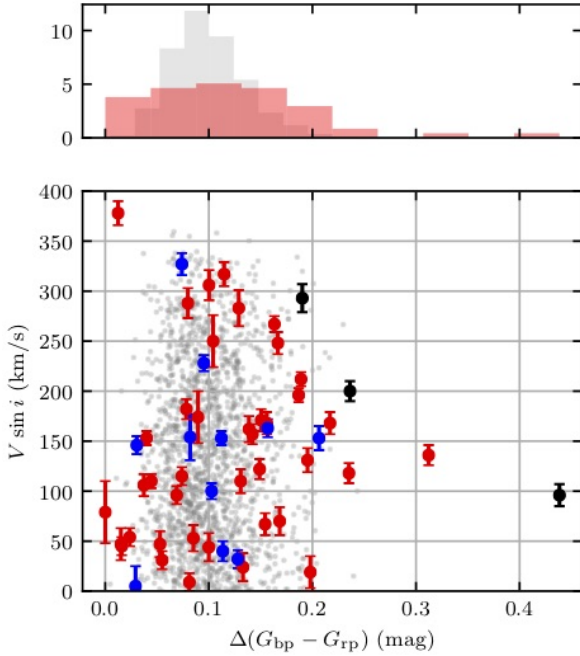


**Figure 10.** (top) Observed  $\Delta(G_{\text{bp}} - G_{\text{rp}})$  distribution (red) and corresponding distribution for the simulated CMD (grey). (bottom)  $\Delta(G_{\text{bp}} - G_{\text{rp}})$ – $V \sin i$  diagram for all stars in NGC 869 with projected rotational velocity measurements, where the red, blue, and black samples represent normal stars, binaries, and possible binaries, as well as emission-line stars. Circles and squares represent stars associated with  $h$  and  $\chi$  Persei, respectively. The background grey dots represent the same distribution for the synthetic cluster. The calculated Spearman’s correlation coefficient between  $\Delta(G_{\text{bp}} - G_{\text{rp}})$  and  $V \sin i$  is 0.22.

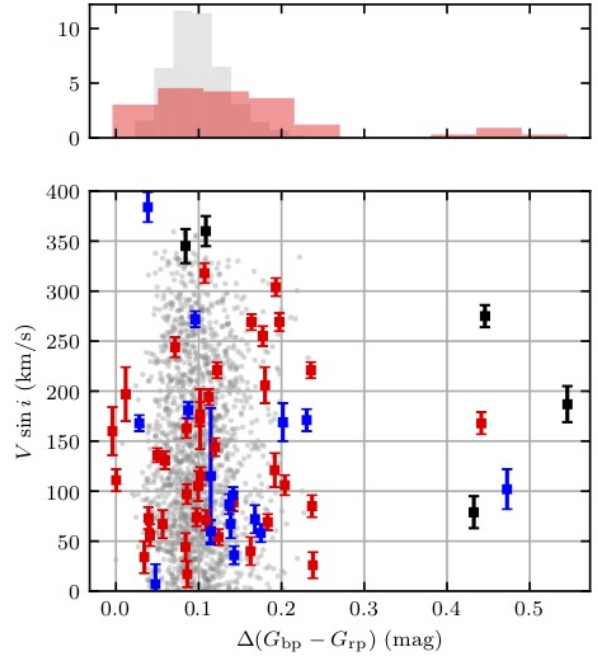


**Figure 11.** As 10, but for NGC 884. The corresponding Spearman’s coefficient is only 0.04

$\Delta(G_{\text{BP}} - G_{\text{rp}}) \geq 0.15$  mag. The number distributions of the color deviation for both the observed and the simulated stars are shown in the top panels of Figures 10 and 11. These histograms also demonstrate that the observed color spreads are more extended than that of the model.

#### 4. DISCUSSION AND SUMMARY

The double clusters  $h$  and  $\chi$  Persei may be the youngest clusters exhibiting eMSTO regions, at an age of only  $\sim 14$  Myr. The eMSTO regions in  $h$  and  $\chi$  Persei are similar to those in other young clusters in the Magellanic Clouds, which cannot be explained by photometric dispersions, differential reddening, internal distance spreads, nor binary contamination. Although both  $h$  and  $\chi$  Persei show apparent eMSTO regions, the complex morphology of their upper MS cannot be explained by multiply aged stellar populations. We found that even if we assume an extended star formation history lasting up to  $\sim 100$  Myr, the extended MS and MSTO regions of  $h$  and  $\chi$  Persei still cannot be well explained.

We have cross matched, respectively, 51 and 55 upper MS stars with reliable measurements of projected rotational velocities in  $h$  and  $\chi$  Persei from the data of Huang & Gies (2006) and Huang et al. (2010), as well as three and five emission-line stars. Most emission-line stars are located on the red side of the MS, which is in line with observational results reported in previous studies of young LMC clusters. However, we do not find any obvious correlation between the colors and projected rotational velocities of the cluster stars.

We compared our observations with a model representing a coeval stellar population characterized by a large range of stellar rotation rates. A simple stellar population with different stellar rotation rates alone cannot fully explain the observed eMSTO regions. The color difference caused by different stellar rotation rates among upper MS stars is negligible compared with the observed width of the MSs and the MSTOs. A statistical analysis shows that the typical color spreads of the observed stars are more extended than implied by the model.

It is unlikely that  $h$  and  $\chi$  Persei are characterized by significant age spreads among their member stars, since their ages and any possible ranges in age have been strongly constrained on the basis of observations in other passbands (e.g., Currie et al. 2010). In addition, we did not find any strong concentration of dust based on the IRAS 100  $\mu\text{m}$  images, indicating that the gas content in these two clusters is very limited (assuming that the gas and dust are spatially co-located). It thus appears that some underlying physical phenomena may have changed the specific stellar colors in the *Gaia* passbands, because the MSs are extended only for  $G \leq 15.5$  mag, which roughly corresponds to stellar masses in excess of  $\sim 1.5$ – $1.6 M_{\odot}$ . This coincides with the mass range where magnetic braking begins to slow down stellar rotation (Georgy et al. 2013).

The inconsistencies between the morphologies of the eMSTO regions in the simulated cluster and the observations may be driven by limitations inherent to the model. As shown by Niederhofer et al. (2015) and Bastian et al. (2018), the extent of the age spread mimicked by stellar rotation is a function of the intrinsic cluster age. For 10–20 Myr-old clusters such as  $h$  and  $\chi$  Persei, the age spread is expected to be only 2–3 Myr (Bastian et al. 2018, their Figure 4). Clearly, the observed width of the eMSTO region would imply an ‘age spread’ that is much more extended than that predicted. This may suggest that there could be a problem in the model’s MSTO calibration for stars in very young clusters. For instance, Be/Oe stars with disks seen edge-on will be reddened by their own disks, an aspect that is not considered in the model. Stars that are observed pole-on will show an excess blue color caused by scattered light off the disk.

D’Antona et al. (2017) advised that blue MS stars are initially rapidly rotating stars that have braked recently. These stars are less advanced in their evolution compared with non-rotating stars with equivalent masses. They suggest that braking of the blue MS stars may be caused by tidal torquing of binary components, indicating that blue upper-MS stars should have binary companions. If this model is valid, there should be a gradient of stellar rotational velocities across the full MS, with stars on the blue side being slowly or non-rotating stars, while stars on the red side would be rapid rotators. Our result does not exhibit such an apparent correlation between the stellar colors and their projected rotational velocities. In addition, the color distribution of binaries and normal stars are similar.

An overlooked role possibly related to the presence of eMSTO regions is convective overshooting. Yang & Tian (2017) calculated the impact of convective overshooting on the MSTO of clusters as young as 100 Myr. They found that adoption of varying overshooting parameters ( $\delta_{\text{ov}}$ ) for individual stars—with  $\delta_{\text{ov}}$  varying from 0.0 to 0.7—can potentially explain the observed eMSTOs in young and intermediate-age clusters. Indeed, variations in stellar overshooting parameters might better mimic an age spread than the presence of different stellar rotation rates, at least for young clusters. This is because convective overshooting is more efficient than rotation at bringing H-rich material into the H-burning core, thus increasing the stellar MS lifetime. In the mean time, terminal-age MS stars with different  $\delta_{\text{ov}}$  may show a spread in nitrogen abundance. This is consistent with some observations, since the MSTO regions of some young clusters are much broader when ultraviolet (UV) observations are involved (e.g.,

F336W/F343N passbands of the *Hubble Space Telescope's* UVIS/WFC3 camera), which are sensitive to nitrogen abundances (e.g., Larsen et al. 2014). Such a nitrogen abundance dispersion cannot be produced by any combination of rotating models with moderate overshooting,  $\delta_{\text{ov}} = 0.2$ , and non-rotating models. This may then be used to differentiate convective core overshooting models from rotation models (Yang & Tian 2017).

Binary interactions may have contributed to form the eMSTO region as well (e.g., Yang et al. 2011; Yang 2018). These authors claim that some of the blue MS and MSTO stars in the CMDs of Magellanic Cloud clusters may be binaries or binary products (including blue straggler stars; BSSs). Using the cluster NGC 1866 as a testbed, Yang (2018) showed that a fraction of the blue MS stars can be explained by either merged stars, MS–naked-He star systems, or MS–white dwarf (WD) systems. In the case of *h* and  $\chi$  Persei, it is unlikely that there will be a population of WD stars because of their young ages. MS–WD systems, if detected, would strongly suggest that these clusters contain a population of stars that are at least  $\sim 30$  Myr old, thus confirming the presence of an internal age spread. The presence of MS–He star systems or binary merger BSSs is more likely. Stars with peculiar colors compared with the ZAMS may be stars that are out of thermal equilibrium and which are probably kept there by being current mass-transfer systems. These stars can be identified by examining if they exhibit W Ursae Majoris-like light curves.

Note that variable stars among the clusters' MS stars may affect the morphology of the CMD. Salinas et al. (2018) tested this scenario for the eMSTO of the cluster NGC 1846 (aged 1–2 Gyr). However, this hypothesis has not been examined for young clusters. A sample of pulsating B-type stars has been detected in both *h* and  $\chi$  Persei (e.g., Krzesiński et al. 1999; Majewska-Świerzbiniowicz et al. 2008; Saesen et al. 2010). Combined with our ongoing survey of variable stars in *h* Persei using the 50 BiN telescope (Xin et al. 2016), we present the distribution of these variable stars in the color–magnitude diagrams (see the left-hand panel of Figure 12). The colors represent the variability amplitudes, with the exception of the three red dots in *h* Persei. The latter are classified as EA-type eclipsing binaries, and all have variability amplitudes greater than 0.15 mag. For  $\chi$  Persei, we directly use the catalog of variable stars provided by Saesen et al. (2010). As shown in Figure 12, although the majority of pulsating stars in these two clusters have relatively small amplitudes, which are unlikely to explain the widths of their MSs, these eclipsing binaries could change their location

along the CMD fairly easily and they could therefore be a possible source of broadened MSs. Note that Saesen et al. (2010) observed variable stars based on multi-site observations with a total exposure time of over 1200 h. The number of variable stars detected in  $\chi$  Persei is higher than the equivalent number in *h* Persei. Given that *h* and  $\chi$  Persei are double clusters with almost identical physical parameters, we conclude that the genuine number of variable stars in *h* Persei should be much higher than that shown in Figure 12.

In summary, the complexity of the MSTO regions in *h* and  $\chi$  Persei may be caused by the combination different underlying physical processes. We also suggest that more detailed models of the stellar rotation of extremely young stellar populations ( $\sim 10$ – $20$  Myr) are required to fully understand the complex MSTO regions in these young clusters.

We thank the anonymous referee for valuable comments. We thank Dr. Yang Wuming at Beijing Normal University for useful discussions. We thank Dr. Yu Heng at Beijing Normal University for his careful review on details of this work. C. L. was supported by the Macquarie Research Fellowship Scheme. This work was supported by the National Key Research and Development Program of China through grant 2017YFA0402702 (RdG). This work was also partly supported by the National Natural Science Foundation of China through grants 11633005 (L. D.), 11373010, 11473037 and 11803048. K. W. acknowledge funding by the China Scholarship Council. This paper has received funding from the European Research Council (ERC) under the European Union's Horizon 2020 research innovation programme (Grant Agreement ERC-StG 2016, No 716082 'GALFOR', PI Milone) and from MIUR through the the FARE project R164RM93XW SEMPLICE (PI Milone).

**This work has made use of data from the European Space Agency (ESA) mission *Gaia* (<https://www.cosmos.esa.int/gaia>), processed by the *Gaia* Data Processing and Analysis Consortium (DPAC, <https://www.cosmos.esa.int/web/gaia/dpac/consortium>). Funding for the DPAC has been provided by national institutions, in particular the institutions participating in the *Gaia* Multilateral Agreement.**

*Facilities:* ESA *Gaia*, Infrared Astronomical Satellite (IRAS, NASA/IPAC)

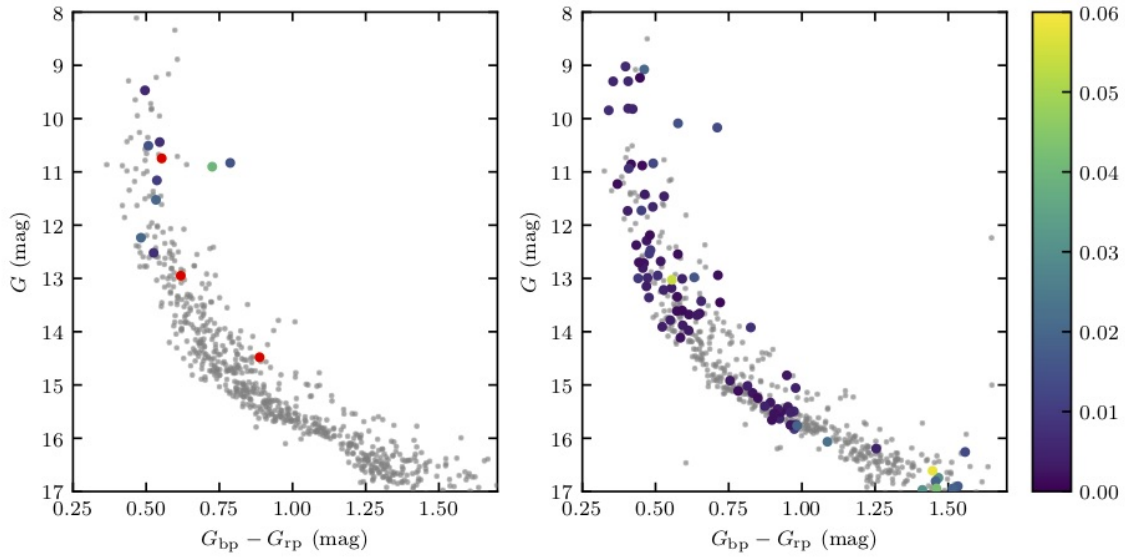


**Figure 12.** CMDs of  $h$  (left) and  $\chi$  Persei (right) with variable stars color-coded by their variability amplitudes. The red dots in  $h$  Persei represent EA-type eclipsing binaries, which have amplitudes of 0.15–0.25 mag.

*Software:* MIST (Paxton et al. 2011, 2013, 2015; Choi et al. 2016; Dotter 2016), TLUSTY and SYNSPEC (Hubeny & Lanz 1995)

## REFERENCES

- Bastian, N., & de Mink, S. E. 2009, MNRAS, 398, L11
- Bastian, N., Kamann, S., Cabrera-Ziri, I., et al. 2018, MNRAS, 480, 3739
- Brandt, T. D., & Huang, C. X. 2015, ApJ, 807, 25
- Brandt, T. D., & Huang, C. X. 2015, ApJ, 807, 24
- Cantat-Gaudin, T., Jordi, C., Vallenari, A., et al. 2018, A&A, 618, A93
- Cardelli, J. A., Clayton, G. C., & Mathis, J. S. 1989, ApJ, 345, 245
- Choi, J., Dotter, A., Conroy, C., et al. 2016, ApJ, 823, 102
- Currie, T., Hernandez, J., Irwin, J., et al. 2010, ApJS, 186, 191
- Cordoni, G., Milone, A. P., Marino, A. F., et al. 2018, ApJ, 869, 139
- D’Antona, F., Milone, A. P., Tailo, M., et al. 2017, Nat. Astron., 1, 0186
- Dotter, A. 2016, ApJS, 222, 8
- Dupree, A. K., Dotter, A., Johnson, C. I., et al. 2017, ApJL, 846, L1
- Espinosa Lara, F., & Rieutord, M. 2011, A&A, 533, A43
- Evans, D. W., Riello, M., De Angeli, F., et al. 2018, A&A, 616, A4
- Gaia Collaboration, Prusti, T., de Bruijne, J. H. J., et al. 2016, A&A, 595, A1
- Gaia Collaboration, Brown, A. G. A., Vallenari, A., et al. 2018, A&A, 616, A1
- Georgy, C., Ekström, S., Eggenberger, P., et al. 2013, A&A, 558, A103
- Georgy, C., Granada, A., Ekström, S., et al. 2014, A&A, 566, A21
- Goudfrooij, P., Girardi, L., & Correnti, M. 2017, ApJ, 846, 22
- Goudfrooij, P., Girardi, L., Bellini, A., et al. 2018, ApJL, 864, L3
- Huang, W., & Gies, D. R. 2006, ApJ, 648, 580
- Huang, W., Gies, D. R., & McSwain, M. V. 2010, ApJ, 722, 605
- Hubeny, I., & Lanz, T. 1995, ApJ, 439, 875
- Kharchenko, N. V., Piskunov, A. E., Schilbach, E., Röser, S., & Scholz, R.-D. 2013, A&A, 558, A53
- Krzeseński, J., Pigulski, A., & Kołaczowski, Z. 1999, A&A, 345, 505
- Larsen, S. S., Brodie, J. P., Grundahl, F., & Strader, J. 2014, ApJ, 797, 15
- Li, C., de Grijs, R., & Deng, L. 2014, Nature, 516, 367
- Li, C., de Grijs, R., Deng, L., & Milone, A. P. 2017, ApJ, 844, 119
- Mackey, A. D., & Broby Nielsen, P. 2007, MNRAS, 379, 151

- Maeder, A., & Meynet, G. 2000, *ARA&A*, 38, 143
- Majewska-Świerzbiniowicz, A., Pigulski, A., Szabó, R., & Csubry, Z. 2008, *J. Phys. Conf. Ser.*, 118, 012068
- Marino, A. F., Milone, A. P., Casagrande, L., et al. 2018, *ApJL*, 863, L33
- Marino, A. F., Przybilla, N., Milone, A. P., et al. 2018, *AJ*, 156, 116
- Milone, A. P., Bedin, L. R., Piotto, G., & Anderson, J. 2009, *A&A*, 497, 755
- Milone, A. P., Bedin, L. R., Piotto, G., et al. 2015, *MNRAS*, 450, 3750
- Milone, A. P., Marino, A. F., D'Antona, F., et al. 2016, *MNRAS*, 458, 4368
- Milone, A. P., Marino, A. F., Di Criscienzo, M., et al. 2018, *MNRAS*, 477, 2640
- Niederhofer, F., Georgy, C., Bastian, N., & Ekström, S. 2015, *MNRAS*, 453, 2070
- O'Donnell, J. E. 1994, *ApJ*, 422, 158
- Paxton, B., Bildsten, L., Dotter, A., et al. 2011, *ApJS*, 192, 3
- Paxton, B., Cantiello, M., Arras, P., et al. 2013, *ApJS*, 208, 4
- Paxton, B., Marchant, P., Schwab, J., et al. 2015, *ApJS*, 220, 15
- Piatti, A. E., & Cole, A. 2017, *MNRAS*, 470, L77
- Saesen, S., Carrier, F., Pigulski, A., et al. 2010, *A&A*, 515, A16.
- Schlafly, E. F., & Finkbeiner, D. P. 2011, *ApJ*, 737, 103
- Saesen, S., Carrier, F., Pigulski, A., et al. 2010, *A&A*, 515, A16
- Salinas, R., Pajkos, M. A., Vivas, A. K., Strader, J., & Contreras Ramos, R. 2018, *AJ*, 155, 183
- Slesnick, C. L., Hillenbrand, L. A., & Massey, P. 2002, *ApJ*, 576, 880
- von Zeipel, H. 1924, *MNRAS*, 84, 665
- Xin, Y., Deng, L., Wang, K., & Tian, J. 2016, *Mem. Soc. Astron. Italiana*, 87, 707
- Yang, W., Meng, X., Bi, S., et al. 2011, *ApJL*, 731, L37
- Yang, W., & Tian, Z. 2017, *ApJ*, 836, 102
- Yang, W. 2018, *ApJ*, 860, 132
- Wu, Z.-Y., Zhou, X., Ma, J., & Du, C.-H. 2009, *MNRAS*, 399, 2146